

Unified Supervision For Vision-Language Modeling in 3D Computed Tomography

Hao-Chih Lee¹ Zelong Liu¹ Hamza Ahmed¹ Spencer Kim¹ Sean Huver²
 Vishwesh Nath² Zahi A. Fayad¹ Timothy Deyer^{3,4} Xueyan Mei¹
¹BioMedical Engineering and Imaging Institute, Icahn School of Medicine at Mount Sinai
² NVIDIA ³East River Medical Imaging ⁴Department of Radiology, Cornell Medicine

Abstract

General-purpose vision-language models (VLMs) have emerged as promising tools in radiology, offering zero-shot capabilities that mitigate the need for large labeled datasets. However, in high-stakes domains like diagnostic radiology, these models often lack the discriminative precision required for reliable clinical use. This challenge is compounded by the scarcity and heterogeneity of publicly available volumetric CT datasets, which vary widely in annotation formats and granularity. To address these limitations, we introduce *Uniferum*, a volumetric VLM that unifies diverse supervision signals, encoded in classification labels and segmentation masks, into a single training framework. By harmonizing three public 3D CT datasets with distinct annotations, *Uniferum* achieves state-of-the-art performance, improving AUROC on the CT-RATE benchmark by 7% compared to CLIP-based and conventional multi-label convolutional models. The model demonstrates robust out-of-distribution generalization, with observed evidence of unexpected zero-shot performance on the RAD-CHEST and INSPECT datasets. Our results highlight the effectiveness of integrating heterogeneous annotations and body segmentation to enhance model performance, setting a new direction for clinically reliable, data-efficient VLMs in 3D medical imaging.

1. Introduction

General-purpose vision-language models (VLMs) have recently attracted widespread attention for their potential to assist in radiology-based diagnosis. VLMs leverage the scale and rich information embedded in paired medical scans and radiology reports. These models demonstrate zero-shot capabilities, the ability that can solve unseen tasks without requiring any labeled data, that can address key limitations of traditional supervised approaches in medical imaging. In particular, contrastive language-image pre-training (CLIP) [18], after being trained on millions of image-text pairs, can be applied “out of the box” to new classification tasks by matching image embeddings to text prompts. This zero-shot approach has sparked interest in medical imaging

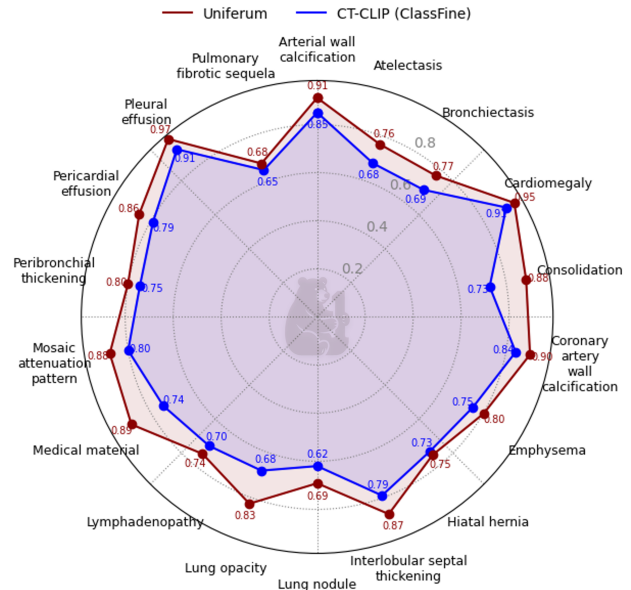


Figure 1. Performance comparison on CT-RATE. We compared Uniferum and CT-CLIP with ClassFinetuning on CT-RATE testing set. Both models were trained solely on CT-RATE.

research, where labeled data is both scarce and costly to obtain.

However, in a high-risk, highly regulated environment such as diagnostic radiology, coarse zero-shot capability alone is insufficient. Clinical decision support tools must meet stringent performance requirements as small differences in sensitivity or specificity can translate into significant patient safety implications. Although CLIP-like models offer broad generalization, their zero-shot outputs frequently lack the fine-tuned discriminative power needed to reliably detect subtle pathologies or to meet predefined performance thresholds in a clinical workflow [23, 31].

How do we go about developing a model of high discriminative power given that volumetric CT images resources, unlike hundreds of millions of natural images available on the Web, are scarce and fragmented? Public volumetric CT datasets rarely

exceed tens of thousands of scans. In addition, each dataset has its own styles and choices of annotations. Some datasets provide structured radiology reports, others supply disease labels of varying granularity, and still others offer segmentation masks for specific organs or lesions. For instance, one dataset might include 18 broad pathological labels, while another lists over 80 more detailed categories of medical findings [4, 6]; many benchmarks focus on segmentation tasks that do not directly translate into classification objectives [17, 22]. The challenge lies in harmonizing all these resources (different datasets with different annotations) in assembling a large scale data set for model development.

To address these challenges, we propose a vision-language model, dubbed Uniferum, that unifies various training signals within one framework. We collect and harmonize three public volumetric CT datasets, each with different annotation labels, and design a training strategy that accommodates multiple supervision modalities. Our model shows superior performance on CT-RATE compared with CLIP based model and standard multi-label volumetric convolutional neural networks. Additionally Uniferum demonstrates surprising zero-shot classification performance on completely with-held datasets. We observed that performance increases with the number of supervised learning tasks. By unifying heterogeneous annotations into a single VLM framework, Uniferum addresses both fragmented data resources and the need for high discriminative power in 3D CT interpretation. This approach paves the way toward clinically reliable, data-efficient vision-language models for radiology.

Our key contributions include

1. We present a framework that unifies diverse supervision signal, including classification labels and segmentation masks, from heterogeneous 3D CT datasets.
2. The proposed volumetric vision-language model that improves the state-of-the-art on CT-RATE by 7% in AUROC. We thoroughly evaluate its performance, both out-of-distribution and zero-shot, on two additional large-scale volumetric CT datasets: RAD-CHEST and INSPECT.
3. Our results demonstrate that the proposed model effectively integrates diverse training signals from both class labels and segmentation masks. Notably, we find that incorporating body segmentation provides a universal strategy for enhancing performance.

The implementation is publicly available at <https://github.com/howchihlee/uniferum>.

2. Related Work

VLM in General Domain: 2D VLM in Radiology

Vision-language models (VLMs) have made significant advances in biomedical imaging, particularly in interpreting two dimensional images such as chest x-ray images. Early efforts, such as CheXpert [10], demonstrated the feasibility of mapping radiology reports to multi-label pathology classification. RadGraph [11] extended the idea by enhancing isolated labels

with a structured knowledge graph, laying the foundation for further evaluation [27] and knowledge-enhanced modeling [30]. Contrastive learning has gained considerable attention in 2D vision-language modeling. BiomedCLIP [29] was pre-trained on a wide range of biomedical imaging tasks using a dataset of 15 million biomedical image-text pairs derived from 4.4 million scientific articles. GLORIA [8] and subsequent models improved upon CLIP by incorporating fine-grained information specific to anatomical regions. MedCLIP [21] introduced semantic matching loss that utilizes entity recognition to estimate semantic similarity between text pairs to mitigate the data hungry issue of CLIP for medical imaging. Particularly relevant to our work, Xu et al. [25] proposed an encoder-decoder multi-task transformer to tackle tasks such as classification, segmentation, and localization. Their model, however, was primarily designed for generative tasks rather than optimized for discriminative performance.

3D volumetric image analysis and vision language modeling

Draeos et al. [4] developed an image-based convolutional neural network on RADCHEST to classify 83 abnormalities. While varying accuracy depending on categories, Draeos et al. demonstrated that performance improved as the number of labels increased. Huang et al. [9] combined ResNetV2 and transformer layers to classify plenary embolism patients and the associated prognostic risks. They found that models integrating both EHR and CT images performed better than single-modality models, while the image-based model performed the worst. Joint classification and segmentation [7, 15, 16] were investigated in the multi-task learning setting and found to perform better when integrating both tasks. Unlike our model, these models rely on paired classification and segmentation masks. Li et al. [13] investigated text-driven segmentation for open-ended segmentation but they did not pursue tasks beyond segmentation.

Hamamci developed generalist models from a multimodal Dataset for 3D CT chest scans and demonstrated clip’s zero-shot classification performs better than supervised convolutional neural networks [6]. Merlin [2], a clip based model, was recently developed based on 15,331 3D CT scans, primarily focused on the abdomen region. There are many other VLM that demonstrate generalist capability but the discriminative power on detecting abnormality from 3D CT scans have not been thoroughly examined [1, 3, 12, 24, 28].

3. Method

3.1. Task format and notations

In this work, we propose a unified model for volumetric medical image analysis that unifies classification and segmentation labels by conditioning on a task-specific natural language description. Let (X, \cdot) denote a volumetric medical image $X \in \mathbb{R}^{n \times m \times s}$ and a supervision labels. We assume that the image volume has either a corresponding binary classification label $y \in \{0, 1\}$ or a paired binary segmentation mask $M \in \{0, 1\}^{n \times m \times s}$, where

each voxel indicates whether it belongs to a structure of interest.

Each input pair is associated with a task description t , which defines the clinical or anatomical objective. For classification, a typical t might be: “Diagnose the presence of coronary artery disease in the heart,” where y indicates presence (1) or absence (0) of the condition. For segmentation, t could be: “Segment the lungs in the image,” where M highlight the regions corresponding to the lungs in the CT scan X . We refer to the tuple $(X, y$ or $M, t)$ as a vision language task in the following text. Note that a single image volume can be associated with multiple labels y and masks M in this context. For example, an image volume with multiple classification labels can be decomposed into several distinct classification tasks, all sharing the same input X . See Section 3.3 for details on how such tasks are constructed from a dataset.

Notably, we do not assume that labels are paired. Neither joint label–mask pairs nor multi-label annotations are required. In multi-label classification, most models estimate a function of the form $f(x) = \mathbf{y} \in \mathbb{R}^k$, where $\mathbf{y} = (y_1, y_2, \dots, y_k)$ is a multi-label output vector. In contrast, we reformulate the problem as estimating a function conditioned on a task-specific description t_i , i.e., $f(x, t_i) = y_i$. This formulation decouples individual label predictions, allowing each sample to be reused across multiple tasks. As a result, the effective training set size increases from n to $n \times k$, and opens up the door to maximizing the utility of fragmented labeled data.

3.2. Model

Our model is an encoder-only VLM that comprises a vision encoder f_v and a transformer f_t that integrates two distinct embedding vectors: one for chest CT volumes and another for task description, respectively (Figure 2). We use $E_v = f_v(X) \in \mathbb{R}^{m/d \times n/d \times s/d}$ where d is the overall factor that downsample the input tensor through the forward propagation. The flattened output of the vision encoder E_v is concatenated with the token embeddings of the task description E_t , along with two additional embedding vectors: a classification token v_{cls} and a separator token v_{sep} . Positional embeddings are added to this sequence before it is passed through a stack of bidirectional transformer layers. The two additional embedding vectors serve as the CLS token for classification and SEP token to separate vision and text embedding respectively. The final output is $E = \text{TransformerLayers}(Z)$ where

$$Z = \text{concat}([v_{\text{cls}}, E_v, v_{\text{sep}}, E_t]) + E_{\text{pos}}.$$

We split E into a vector and a sequence of embeddings. The first is the transformed CLS embedding vector E_{cls} which is positioned at the first entry of E . The following $r = mns/d^3$ vectors in E form a sequence denoted as $E_s \in \mathbb{R}^{r \times f_h}$, which serves as embeddings to predict segmentation mask. f_h is the dimension of hidden space.

For classification tasks, we passed E_{cls} into a linear layer to transform it into a prediction logit, where binary cross-entropy

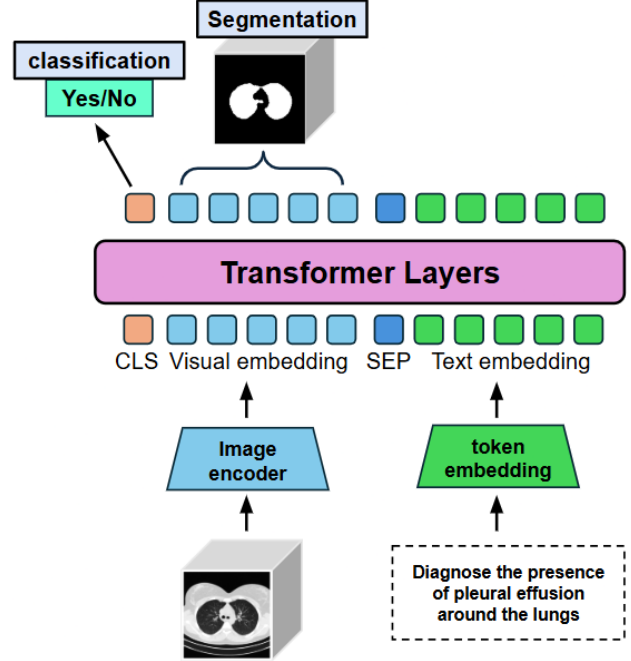


Figure 2. model architecture of Uniferum.

is used for model training. For segmentation tasks, we apply a linear layer to the segmentation embeddings E_s to predict a binary mask. While this method is straightforward, it must address two main challenges. First, predicting full-resolution 3D volumetric images is memory-intensive. Second, the 3D convolutional encoder reduces spatial resolution by a factor of d (the downsampling factor). To balance these constraints, we adopt a linear layer that up-samples the segmentation embeddings E_s to an intermediate resolution.

Specifically, we first apply a max pooling operation with filter size d/u to the ground truth binary mask. We then divide the volume into non-overlapping patches of size $u \times u \times u$, flatten each patch, and stack them into a binary target array of shape $(mns/d^3, u^3)$. Accordingly, the linear layer is designed to map each embedding in E_s to a vector of size u^3 , producing an output that aligns with the target patch-wise representation. Although our goal is not to produce fine-grained segmentation, but rather to integrate fine-grained localization information into the classification model, the final output can still be unpacked for visualization purposes.

During model training, we mixed classification and segmentation in one batch and calculated loss only for the task whose target label is available. Binary cross-entropy was used for classification tasks, while focal loss [14] was applied to measure the discrepancy between predicted logits and the target masks in segmentation tasks. To address the issue that focal loss values can diminish rapidly during training, we scaled the focal loss by a factor of 10.

3.3. Creating training data

Designing and creating training data is a critical part of our work. For each label in the dataset we create a task description. We categorize tasks in the following three groups:

1. For diagnostic tasks we used the template “Diagnose the presence of [label name] in/around the [organ]” to generate the task description. For example, for the label of pleural effusion, the task description associated with it is “Diagnose the presence of pleural effusion around the lungs”. We reviewed and reformatted the labels into readable text if necessary.
2. For prognostic tasks, we used the template “Predict the risk of [label name] in [x months]”. For example, “Predict the risk of mortality in 6 months” describes the 6-month mortality label in INSPECT.
3. For segmentation tasks, we apply the template “Segment [label name] in the image.” We generate 60 organ segmentation tasks that include 53 labels predicted by TotalSegmentator and 7 derived tasks by combining TotalSegmentator labels into general categories such as “ribs” and “lungs”. We include an additional nodule segmentation task using 601 masks from the LUNA16[17] dataset.

To handle the issue of sample imbalance, we randomly sampled negative examples to match the number of positive examples for each diagnostic and prognostic task. Additionally, we randomly sampled an extra 10% samples from the dataset to assign an organ segmentation task. We upsampled the LUNA16 samples tenfold to a total of 6,010 samples as an add-on for datasets augmented with segmentation tasks.

3.4. Datasets

We utilized three publicly available 3D CT datasets, including CT-RATE, RAD-CHEST, and INSPECT, for model development and benchmarking. Each dataset provides volumetric imaging data along with task-specific annotations. Below, we summarize the key statistics of three dataset in table 1 and describe the datasets in detail below:

3.4.1. CT-RATE

CT-RATE [6] is a large-scale dataset of 50,188 non-contrast 3D chest CT volumes paired with full-text radiology reports, collected from 25,692 distinct CT studies conducted on 21,034 unique patients. Each CT volume is accompanied by a radiologist-authored report, which includes structured sections such as Impression, Findings, Patient Information, and Scan Technique as well as 18 pathology labels (see table 1 in Appendix). Scans of 100 patients from the official training set were withheld for model selection. We used the official validation set of 3002 volumes from 1,564 studies to calculate the final metrics while filtering out all brain scans.

3.4.2. RAD-CHEST

RAD-ChestCT [4] is a large-scale dataset comprising 36,000 chest CT scans from 20K unique patients. However, the current

release includes an initial subset of 3,630 scans, representing roughly 10% of the full dataset. Each scan is annotated with 84 abnormalities across 52 anatomical locations extracted from radiology reports. We selected 39 abnormality labels related to the lungs, opacity patterns, and the heart, as categorized in the RAD-Chest paper (see Table 1 in Appendix). We further categorized these 39 abnormality labels into 32 RAD-Chest-unique labels not present in the CT-RATE labels, and 7 shared labels that overlap with the CT-RATE labels for benchmarking.

3.4.3. INSPECT

INSPECT [9] is a large-scale, multimodal dataset designed to enable research on integrating 3D CT pulmonary angiography (CTPA) with structured clinical data for pulmonary embolism (PE) patients. It includes de-identified longitudinal records from 19,438 patients, comprising 20,078 CT scans, 21,266 radiology report impression sections, and structured EHR data. In contrast to the other two datasets that are primarily diagnosis focused, INSPECT provides 1 diagnostic label (pulmonary embolism) and 7 prognostic labels (see table 1 in appendix). We note that the CT pulmonary angiography was performed with a contrast agent. At the time of writing, the information of the cohort hasn’t been made public. We thus split the dataset in 15148, 1000, 3000 scans for training, validation and testing respectively to be consistent with the setting in INSPECT [9]. We dropped 145 scans that either had a corrupted affine matrix or dual channels. The percentage of positive labels of our validation splits are consistent with those reported by INSPECT [9].

In addition to these labels, we further generated 12 diagnosis labels as additional benchmarking (see table 1 in appendix). For these labels, we first applied keyword matching to locate a subset of reports that potentially include direct mention of the abnormality. We then randomly sampled equal numbers of reports as potential negatives. We then prompted gpt-4o-mini to validate the presence of the abnormality based on the impression and used these generated labels for validation (See the prompt in Appendix Table 2). A senior radiologist reviewed 120 samples, 10 per class randomly sampled, and found 115 (96%) of those annotations were accurate. Since only the impression sections were available, we used word clouds for visualization and selected diagnosis labels that were frequently mentioned in the corpus. However, labels such as ‘nodules’ may include false negatives that cannot be identified based solely on the impression section.

Table 1. Summary of Three Primary Datasets. See section 3.3 and appendix table 1 for definitions of shared and unique tasks.

	Number of CT Scans			Number of Tasks	
	Train	Validation	Test	Shared	Unique
CT-RATE	46168	221	3002	18	–
INSPECT	15148	1000	3000	12	6
RADCHEST	2286	984	360	7	32

3.5. Imaging preprocessing

All images were first converted to the NIfTI format when not originally downloaded in this format. Voxel intensities were standardized to Hounsfield Units (HU) and clipped to the range from -1000 to 1000 to suppress extreme outliers. Full-body segmentation was applied to each image scan using Total Segmentator, except for those from CT-RATE, for which we used the provided segmentation to ensure reproducibility. Images were cropped and centered using the following workflow: a thresholding operation was applied to the soft-tissue channel (HU -150 to 250) to identify the largest connected component. A convex hull transformation was then applied on each axial slice to estimate a common center of mass in the x-y plane. Image slices that are 5 mm away in the z axis from the top/bottom of the lung, identified by total Segmentator, were discarded. The voxel size was normalized to 1 mm x 1 mm x 1 mm. We cropped or padded when necessary to make images to 416 mm in x, 336 mm in y and 256 mm in z. During training we applied augmentations including random rotation up to ± 15 degree, random zooming up to 10% as well as adding Gaussian noise and random offset in pixel intensity. CT volumes were then center cropped to a volume of 384 mm x 320 mm x 256 mm and resized to a 256 x 160 x 128 array for training and inference.

3.6. Model training details

We use EfficientNet b0 [20] as the backbone for the vision encoder. The vision encoder was initialized with 2D model weights pretrained on ImageNet. The weights were inflated to adapt for 3D input by extending the 2D convolutional filters into the third dimension [19]. Specifically, each 2D filter (e.g., a 3x3 kernel) was replicated along the depth axis to form a 3D kernel (e.g., a 3x3x3 filter), effectively copying the same weights across the third dimension.

We used 4 stacked attention layers to integrate vision embeddings and text embeddings. We initialized the weights using the first 4 layers of PubMedBert [5]. AdamW was used as the optimizer with linearly decaying step sizes and 25 warm-up steps. As each dataset has different sample sizes, we iterated the model training for 25,000 steps with a batch size of 64 samples for most of our experiments while we keep track of validation metrics for every 5000 steps. For experiments that use only RADCHEST and INSPECT with significantly less vision-language task samples, we iterated for 10,000 steps with a batch size of 64 samples and keep track of validation metrics for every 1000 steps. Models were selected based on the best average Area under ROC curve (AUROC) across validation tasks. We trained our models on a single H100 GPU and most experiments were done in 24 hours.

4. Experiments

We trained models on various dataset configurations, including three standalone datasets CT-RATE, INSPECT and RAD-

CHEST. We also trained models on combinations such as CT-RATE + INSPECT or CT-RATE + RADCHEST, and combined data that incorporated additional segmentation tasks. The notation CT-RATE + INSPECT denotes a combination of datasets, while +SEG indicates that segmentation tasks were included during training. All models were trained with 25,000 iterations with exception that INSPECT and RADCHEST alone were trained for 10,000 iterations. Table 1 summarizes the key characteristics of each dataset.

We then evaluated the classification accuracies on each dataset. For INSPECT and RADCHEST, we divided the tasks into two categories: those shared with CT-RATE as external validation to access out-of-distribution generalization, and those unique to each dataset for zero-shot validation. We evaluate the performance by the average area under ROC curve (AUROC) and the area under the precision-recall curve (AUPR) for each category.

For comparison, we implemented a baseline using a 3D EfficientNet-b0 backbone from the timm-3d library. The architecture includes depthwise separable convolutions, squeeze-and-excitation blocks, and global average pooling, followed by a classification head with two dropout layers and an intermediate ReLU activation. The model outputs a vector of logits, one per task, with each task trained independently using binary cross entropy. Optimization was performed using AdamW with a ReduceLRonPlateau learning rate scheduler. The same image augmentations were applied during training. Performance was evaluated using Area under the ROC curve (AUROC) and Area under the precision-recall curve (AUPR) using the same sample splits.

5. Results

Table 2 summarizes the average area under the ROC curve (AUROC) for our results. We also list the average area under the precision-recall curve in Appendix Table 3. We present our observations below based on AUROC, due to its robustness to the number of labels and the ease of cross-referencing performance reported in the literature. We include the AUROC for each individual category in Appendix Figures 1, 2, and 3.

5.1. Performance Comparison of Models Trained on a individual dataset

We observe that Uniferum outperforms other models across multiple datasets. On the CT-RATE dataset, Uniferum achieved an average AUROC improvement of 7% over CT-CLIP (83.0% v.s. 75.6%) and 20% over CT-NET, a convolutional neural networks model (83.0% v.s. 62.9%).

On the INSPECT dataset, Uniferum demonstrated a 10% improvement over convolutional neural networks (71% v.s. 61%). Uniferum demonstrated 6% improvement in auroc compared to the image only model reported in INSPECT [9] (71% v.s. 65.9%), despite underperforming in diagnosing pulmonary embolism (64.8% v.s. 72.1%). We note that, since

Table 2. Average Area Under the ROC Curve (AUROC)

Model	Training Dataset	CTRATE	INSPECT		RADCHEST	
			Shared	Unique	Shared	Unique
Uniferum	CTRATE	0.8296	0.7207	0.5808	0.7960	0.5559
	CTRATE+SEG	0.8311	0.7436	0.6130	0.8009	0.5768
	CTRATE+INSPECT	0.8241	0.7186	0.7318	0.7933	0.5974
	CTRATE+INSPECT+SEG	0.8298	0.6977	0.7383	0.8022	0.6077
	CTRATE+RADCHEST	0.8286	0.7347	0.5929	0.8143	0.7417
	CTRATE+RADCHEST+SEG	0.8305	0.7582	0.6124	0.8249	0.7512
	INSPECT	0.6431	0.5584	0.7158	0.6097	0.5800
	RADCHEST	0.7006	0.6379	0.4993	0.7668	0.6673
CNN	INSPECT	–	–	0.6132	–	–
	RADCHEST	–	–	–	0.700	0.634
CT-NET	CTRATE	0.6291 ¹	–	–	–	–
CT-CLIP (zero-shot)	CTRATE	0.7311 ¹	–	–	–	–
CT-CLIP (vocabFine)	CTRATE	0.7561 ¹	–	–	–	–
CT-CLIP (classFine)	CTRATE	0.7561 ¹	–	–	–	–
CNN+Transformer	INSPECT	–	–	0.6585 ²	–	–
CNN	RADCHEST	–	–	–	0.8353 ³	–

¹ Results from Hamamci et al. [6]

² Results from Huang et al. [9] We note that the model was trained and evaluated on splits different from ours.

³ Results from Draelos et al. [4] The model was trained on the data set 10 fold larger than publicly released.

the details of the INSPECT cohort have not been publicly released, we conducted evaluation using our own train-test split. Therefore, performance metrics may not be directly comparable to those reported in INSPECT [9].

On the RADCHEST dataset, Uniferum outperformed our own CNN baseline by 6% (76.7% v.s. 70.0% on RADCHEST-shared, 66.7% v.s. 63.4% on RADCHEST-unique). However, its performance was slightly lower than the results of the CNN model reported in RADCHEST [4] (76.7% v.s. 83.5% on RADCHEST shared tasks). We emphasize that, because only 10% of the RADCHEST samples were publicly available for training and evaluation, these comparisons should be interpreted with caution.

5.2. Performance Comparison of Models Trained on Dataset Combinations

We generally observed improved performance when incorporating additional datasets alongside CT-RATE. When comparing models trained on CT-RATE alone versus CT-RATE

+ INSPECT, performance remained comparable on tasks shared with CT-RATE. However, we observed a 4% improvement on tasks unique to RADCHEST. A similar trend was observed when comparing CT-RATE to CT-RATE + RADCHEST: performance on CT-RATE tasks remained stable, while there was a 1% improvement on classification tasks, both those shared with and unique to INSPECT. We also found that including segmentation tasks consistently improved performance by 1–3% compared to counterparts trained without segmentation. This held true for both shared-task validation and zero-shot scenarios. Notably, these segmentation tasks were derived from CT scans, suggesting that adding body segmentation represents a broadly applicable and low-cost method to enhance classification performance. Surprisingly, despite intentionally including the LUNA16 dataset that provides fine-grained lung nodule localization, we did not observe any performance gain in predicting the presence of lung nodules (see Appendix Table 4).

To demonstrate robustness, we observed similar patterns when replacing the pretrained attention layers with the first

four layers of GatorTron-base [26], a model pretrained on clinical notes rather than scientific literature. Detailed results are reported in the appendix table 5.

5.3. Evaluating Out-of-Distribution Generalization of Uniferum

To assess cross-dataset generalizability, we evaluated the model on tasks common to multiple datasets. Specifically, we trained models exclusively on CT-RATE and assessed their performance using samples with the same labels from INSPECT and RADCHEST. The model achieved an AUROC of 83.0% on CT-RATE, indicating strong out-of-distribution performance. When applied to related tasks in INSPECT, the AUROC dropped to 72.1%, reflecting a moderate decline in generalization performance. On RADCHEST, the model achieved an AUROC of 79.6%, suggesting better cross-dataset generalization than on INSPECT.

5.4. Evaluating Zero-Shot Classification of Uniferum

To assess the capability of zero-shot classification, we evaluated the model on tasks that are unique to each individual dataset. Specifically, we applied models trained on CT-RATE and assessed their performance on seven prognostic tasks and one pulmonary embolism classification task in INSPECT, as well as 32 nuanced classification labels in RADCHEST. Though we did not expect strong zero-shot performance, the model was able to achieve reasonable performance on certain zero-shot tasks (Figure 3 and 4) performing on par with or better than CNN baseline trained on in-distribution datasets. For example, the model trained on CT-RATE was able to predict 1-month, 6-month and 12 month in-hospital mortality with $71.6 \pm 3.9\%$, $69.5 \pm 2.9\%$ and $68.2 \pm 2.8\%$ AUROC, as well as such unseen diagnostic tasks such as the presence of honeycombing pattern ($69.2 \pm 11.0\%$ AUROC, 10 positives out of 360 samples), coronary artery bypass grafting ($74.8 \pm 9.1\%$ AUROC, 16 positives out of 360 samples) and pacemaker/defib ($90.5 \pm 7.7\%$ AUROC, 17 positives out of 360 samples) in RADCHEST. Such zero-shot capability could be raised by adding body segmentation tasks (Figure 3 and 4). For example, when trained on CTRATE+SEG dataset, the performance changes to $65.0 \pm 13.0\%$, $80.3 \pm 5.2\%$, $92.7 \pm 5.2\%$ for predicting honeycombing pattern, coronary artery bypass grafting and pacemaker/defib, despite the improvement not statistically significant. Similarly, when evaluated on INSPECT, the performance improves to $75.6 \pm 3.8\%$ ($p=0.20$), $75.6 \pm 2.5\%$ ($p=0.03$), $74.2 \pm 2.5\%$ ($p=0.02$) for 1, 6 and 12 month mortality respectively, with the inclusion of additional body segmentation tasks. The 95% confidence intervals and p-values above were calculated using DeLong’s method. We include the AUROC for each individual category in Appendix Figures 1, 2, and 3.

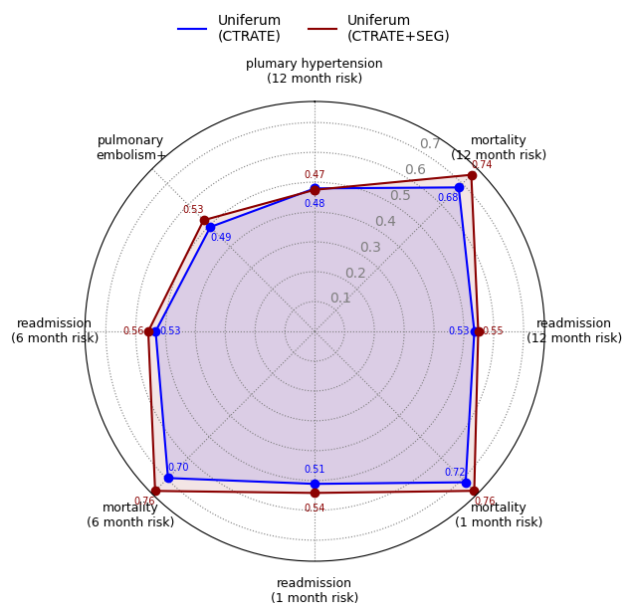


Figure 3. Zero-shot performance on INSPECT. Models were trained on CT-RATE with (red) and without (blue) body segmentation tasks and evaluated on tasks that are not included in CT-RATE.

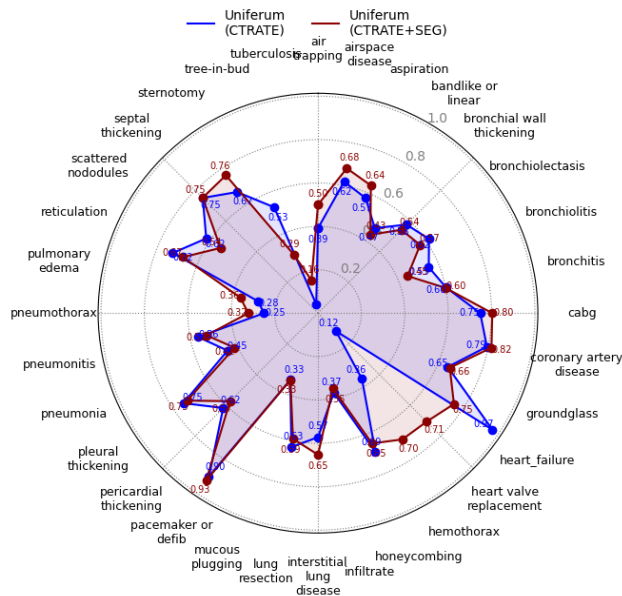


Figure 4. Zero-shot performance on RADCHEST. Models were trained on CT-RATE with (red) and without (blue) body segmentation tasks and evaluated on tasks that are not included in RADCHEST.

6. Conclusion

In this work, we present Uniferum, a volumetric vision-language model designed to overcome key limitations in medical imaging by unifying heterogeneous annotation types within a single training framework. By harmonizing multiple public 3D CT datasets and incorporating both classification and segmentation supervision, Uniferum demonstrates substantial gains in discriminative performance over existing models.

Our experiments show that Uniferum achieves 83% in AUROC across 18 CT-RATE abnormality predictions, outperforming both CLIP-based baselines and standard multi-label CNNs. Additionally, Uniferum maintains strong generalization ability, achieving 72% and 79% AUROC on out-of-distribution datasets RAD-CHEST and INSPECT respectively. Notably, we observe that adding body segmentation tasks contributes to 1-3% performance gains, highlighting the value of integrating diverse supervision signals.

These findings underscore the importance of flexible training strategies in high-stakes domains like radiology. By enabling robust and data-efficient learning from fragmented and variably annotated datasets, Uniferum represents a step toward clinically viable vision-language models for 3D CT interpretation. Future work will focus on scaling to additional modalities, enhancing cross-task synthesis and validating performance in real-world clinical workflows. For those about to fight for VLM, diverse supervision signals abound in public volumetric datasets.

Acknowledgment This work was supported by Scientific Computing and Data at the Icahn School of Medicine at Mount Sinai and NIH grants UL1TR004419, S10OD026880, and S10OD030463. XM is supported by the Eric and Wendy Schmidt AI in Human Health Fellowship, a program of Schmidt Sciences. This research used data provided by the Stanford Center for Artificial Intelligence in Medicine and Imaging (AIMI).

References

- [1] Fan Bai, Yuxin Du, Tiejun Huang, Max Q-H Meng, and Bo Zhao. M3d: Advancing 3d medical image analysis with multi-modal large language models. *arXiv preprint arXiv:2404.00578*, 2024.
- [2] Louis Blankemeier, Joseph Paul Cohen, Ashwin Kumar, Dave Van Veen, Syed Jamal Safdar Gardezi, Magdalini Paschali, Zhihong Chen, Jean-Benoit Delbrouck, Eduardo Reis, Cesar Truys, et al. Merlin: A vision language foundation model for 3d computed tomography. *arXiv preprint arXiv:2406.06512*, 2024.
- [3] Hao Chen, Wei Zhao, Yingli Li, Tianyang Zhong, Yisong Wang, Youlan Shang, Lei Guo, Junwei Han, Tianming Liu, Jun Liu, et al. 3d-ct-gpt: Generating 3d radiology reports through integration of large vision-language models. *arXiv preprint arXiv:2409.19330*, 2024.
- [4] Rachel Lea Draelos, David Dov, Maciej A Mazurowski, Joseph Y Lo, Ricardo Henao, Geoffrey D Rubin, and Lawrence Carin. Machine-learning-based multiple abnormality prediction with large-scale chest computed tomography volumes. *Medical image analysis*, 67:101857, 2021.
- [5] Yu Gu, Robert Tinn, Hao Cheng, Michael Lucas, Naoto Usuyama, Xiaodong Liu, Tristan Naumann, Jianfeng Gao, and Hoifung Poon. Domain-specific language model pretraining for biomedical natural language processing. *ACM Transactions on Computing for Healthcare (HEALTH)*, 3(1):1–23, 2021.
- [6] Ibrahim Ethem Hamamci, Sezgin Er, Furkan Almas, Ayse Gulnihhan Simsek, Sevval Nil Esirgun, Irem Dogan, Muhammed Furkan Dasdelen, Omer Faruk Durugol, Bastian Wittmann, Tamaz Amiranashvili, et al. Developing generalist foundation models from a multimodal dataset for 3d computed tomography. *arXiv preprint arXiv:2403.17834*, 2024.
- [7] Xiaoyu He, Yong Wang, Shuang Zhao, and Xiang Chen. Joint segmentation and classification of skin lesions via a multi-task learning convolutional neural network. *Expert Systems with Applications*, 230:120174, 2023.
- [8] Shih-Cheng Huang, Liyue Shen, Matthew P Lungren, and Serena Yeung. Gloria: A multimodal global-local representation learning framework for label-efficient medical image recognition. In *Proceedings of the IEEE/CVF international conference on computer vision*, pages 3942–3951, 2021.
- [9] Shih-Cheng Huang, Zepeng Huo, Ethan Steinberg, Chia-Chun Chiang, Curtis Langlotz, Matthew Lungren, Serena Yeung, Nigam Shah, and Jason Fries. Inspect: a multimodal dataset for patient outcome prediction of pulmonary embolisms. *Advances in Neural Information Processing Systems*, 36:17742–17772, 2023.
- [10] Jeremy Irvin, Pranav Rajpurkar, Michael Ko, Yifan Yu, Silviana Ciurea-Ilcus, Chris Chute, Henrik Marklund, Behzad Haghighi, Robyn Ball, Katie Shpanskaya, et al. Chexpert: A large chest radiograph dataset with uncertainty labels and expert comparison. In *Proceedings of the AAAI conference on artificial intelligence*, pages 590–597, 2019.
- [11] Saahil Jain, Ashwin Agrawal, Adriel Saporta, Steven QH Truong, Du Nguyen Duong, Tan Bui, Pierre Chambon, Yuhao Zhang, Matthew P Lungren, Andrew Y Ng, et al. Radgraph: Extracting clinical entities and relations from radiology reports. *arXiv preprint arXiv:2106.14463*, 2021.
- [12] Haoran Lai, Zihang Jiang, Qingsong Yao, Rongsheng Wang, Zhiyang He, Xiaodong Tao, Wei Wei, Weifu Lv, and S Kevin Zhou. E3d-gpt: Enhanced 3d visual foundation for medical vision-language model. *arXiv preprint arXiv:2410.14200*, 2024.
- [13] Yuheng Li, Yuxiang Lai, Maria Thor, Deborah Marshall, Zachary Buchwald, David S Yu, and Xiaofeng Yang. Towards universal text-driven ct image segmentation. *arXiv preprint arXiv:2503.06030*, 2025.
- [14] Tsung-Yi Lin, Priya Goyal, Ross Girshick, Kaiming He, and Piotr Dollár. Focal loss for dense object detection. In *Proceedings of the IEEE international conference on computer vision*, pages 2980–2988, 2017.
- [15] Yaling Lu, Fengyuan Sun, Jingyu Wang, and Kai Yu. Automatic joint segmentation and classification of breast ultrasound images via multi-task learning with object contextual attention. *Frontiers in Oncology*, 15:1567577, 2025.
- [16] Sachin Mehta, Ezgi Mercan, Jamen Bartlett, Donald Weaver, Joann G Elmore, and Linda Shapiro. Y-net: joint segmentation and classification for diagnosis of breast biopsy images. In *International conference on medical image computing and computer-assisted intervention*, pages 893–901. Springer, 2018.

- [17] Keelin Murphy, Bram van Ginneken, Arnold MR Schilham, BJ De Hoop, Hester A Gietema, and Mathias Prokop. A large-scale evaluation of automatic pulmonary nodule detection in chest ct using local image features and k-nearest-neighbour classification. *Medical image analysis*, 13(5):757–770, 2009.
- [18] Alec Radford, Jong Wook Kim, Chris Hallacy, Aditya Ramesh, Gabriel Goh, Sandhini Agarwal, Girish Sastry, Amanda Askell, Pamela Mishkin, Jack Clark, et al. Learning transferable visual models from natural language supervision. In *International conference on machine learning*, pages 8748–8763. PMLR, 2021.
- [19] Roman Solovyev, Alexandr A Kalinin, and Tatiana Gabruseva. 3d convolutional neural networks for stalled brain capillary detection. *Computers in biology and medicine*, 141:105089, 2022.
- [20] Mingxing Tan and Quoc Le. Efficientnet: Rethinking model scaling for convolutional neural networks. In *International conference on machine learning*, pages 6105–6114. PMLR, 2019.
- [21] Zifeng Wang, Zhenbang Wu, Dinesh Agarwal, and Jimeng Sun. Medclip: Contrastive learning from unpaired medical images and text. In *Proceedings of the Conference on Empirical Methods in Natural Language Processing. Conference on Empirical Methods in Natural Language Processing*, page 3876, 2022.
- [22] Jakob Wasserthal, Hanns-Christian Breit, Manfred T Meyer, Maurice Pradella, Daniel Hinck, Alexander W Sauter, Tobias Heye, Daniel T Boll, Joshy Cyriac, Shan Yang, et al. Totalsegmentator: robust segmentation of 104 anatomic structures in ct images. *Radiology: Artificial Intelligence*, 5(5), 2023.
- [23] Stefano Woerner and Christian F Baumgartner. Navigating data scarcity using foundation models: A benchmark of few-shot and zero-shot learning approaches in medical imaging. In *International Workshop on Foundation Models for General Medical AI*, pages 30–39. Springer, 2024.
- [24] Chaoyi Wu, Xiaoman Zhang, Ya Zhang, Yanfeng Wang, and Weidi Xie. Towards generalist foundation model for radiology. *arXiv preprint arXiv:2308.02463*, 2023.
- [25] Lijian Xu, Ziyu Ni, Xinglong Liu, Xiaosong Wang, Hongsheng Li, and Shaoting Zhang. Learning a multi-task transformer via unified and customized instruction tuning for chest radiograph interpretation. *arXiv preprint arXiv:2311.01092*, 2023.
- [26] Xi Yang, Aokun Chen, Nima PourNejatian, Hoo Chang Shin, Kaleb E Smith, Christopher Parisien, Colin Compas, Cheryl Martin, Anthony B Costa, Mona G Flores, et al. A large language model for electronic health records. *NPJ digital medicine*, 5(1): 194, 2022.
- [27] Feiyang Yu, Mark Endo, Rayan Krishnan, Ian Pan, Andy Tsai, Eduardo Pontes Reis, Eduardo Kaiser Ururahy Nunes Fonseca, Henrique Min Ho Lee, Zahra Shakeri Hossein Abad, Andrew Y Ng, et al. Evaluating progress in automatic chest x-ray radiology report generation. *Patterns*, 4(9), 2023.
- [28] Haiyang Yu, Siyang Yi, Ke Niu, Minghan Zhuo, and Bin Li. Umit: Unifying medical imaging tasks via vision-language models. *arXiv preprint arXiv:2503.15892*, 2025.
- [29] Sheng Zhang, Yanbo Xu, Naoto Usuyama, Hanwen Xu, Jaspreet Bagga, Robert Tinn, Sam Preston, Rajesh Rao, Mu Wei, Naveen Valluri, et al. Biomedclip: a multimodal biomedical foundation model pretrained from fifteen million scientific image-text pairs. *arXiv preprint arXiv:2303.00915*, 2023.
- [30] Xiaoman Zhang, Chaoyi Wu, Ya Zhang, Weidi Xie, and Yanfeng Wang. Knowledge-enhanced visual-language pre-training on chest radiology images. *Nature Communications*, 14(1):4542, 2023.
- [31] Ximiao Zhang, Min Xu, Dehui Qiu, Ruixin Yan, Ning Lang, and Xiuzhuang Zhou. Medclip: Adapting clip for few-shot medical image anomaly detection. In *International Conference on Medical Image Computing and Computer-Assisted Intervention*, pages 458–468. Springer, 2024.

Unified Supervision For Vision-Language Modeling in 3D Computed Tomography

Supplementary Material

Table 1. List of tasks for training and validation.

CTRATE	Arterial wall calcification, Atelectasis, Bronchiectasis, Cardiomegaly, Consolidation, Coronary artery wall calcification, Emphysema, Hiatal hernia, Interlobular septal thickening, Lung nodule, Lung opacity, Lymphadenopathy, Medical material, Mosaic attenuation pattern, Peribronchial thickening, Pericardial effusion, Pleural effusion, Pulmonary fibrotic sequela
INSPECT (shared)	12_month_PH, 12_month_mortality, 12_month_readmission, 1_month_mortality, 1_month_readmission, 6_month_mortality, 6_month_readmission, pe_positive
INSPECT (unique)	Atelectasis, Bronchiectasis, Cardiomegaly, Consolidation, Coronary artery wall calcification, Emphysema, Hiatal hernia, Interlobular septal thickening, Lung nodule, Peribronchial thickening, Pericardial effusion, Pleural effusion
RADCHEST (shared)	Atelectasis, Bronchiectasis, Cardiomegaly, Consolidation, Emphysema, Pericardial effusion, Pleural effusion
RADCHEST (unique)	Air trapping, Airspace disease, Aspiration, Bandlike or linear, Bronchial wall thickening, Bronchiolectasis, Bronchiolitis, Bronchitis, CABG, Coronary artery disease, Ground-glass, Heart failure, Heart valve replacement, Hemothorax, Honeycombing, Infiltrate, Interstitial lung disease, Lung resection, Mucous plugging, Pacemaker or defib, Pericardial thickening, Pleural thickening, Pneumonia, Pneumonitis, Pneumothorax, Pulmonary edema, Reticulation, Scattered nodules, Septal thickening, Sternotomy, Tree-in-bud, Tuberculosis
Body segmentation tasks	Liver, Stomach, Left upper pulmonary lobe, Left lower pulmonary lobe, Right upper pulmonary lobe, Right middle pulmonary lobe, Right lower pulmonary lobe, Esophagus, Tracheal airway, Thoracic vertebra 1-12, Cardiac organ, Thoracic aorta, Pulmonary vein, Left atrial appendage, Superior vena cava, Inferior vena cava, Left rib 1-12, Right rib 1-12, Sternal body, Costal cartilaginous structures, Lungs, Thoracic vertebrae, Ribs, Right ribs, Left ribs

Table 2. Prompt for identifying presence of abnormality in radiology reports.

Please review the radiology report and identify any findings indicative of{PATHOLOGY}, focusing on the lung region and heart. Return the following in a structured JSON format:

```

{{
  "KeySentence": "Provide the key sentence in the report that supports your answer. If no relevant sentences, return 'NONE'",
  "PresenceOfPathology": "Answer with 'Yes' or 'No' based on the presence of{PATHOLOGY}. If no pathology is mentioned, assume 'No'."
}}

```

Return nothing else.

Below is the report:
{REPORT}

Table 3. Performance comparison on classifying Lung nodules

model	training dataset	val dataset	auroc
Uniferum	CTRATE	CTRATE (Lung nodules)	0.6915
	CTRATE+SEG	CTRATE (Lung nodules)	0.6791
	CTRATE+INSPECT	CTRATE (Lung nodules)	0.6838
	CTRATE+INSPECT+SEG	CTRATE (Lung nodules)	0.68
	CTRATE+RADCHEST	CTRATE (Lung nodules)	0.6873
	CTRATE+RADCHEST+SEG	CTRATE (Lung nodules)	0.6884
	INSPECT	CTRATE (Lung nodules)	0.4891
	RADCHEST	CTRATE (Lung nodules)	0.463

Table 4. Average AUROCs of Uniferum initialized by GatorTron

training dataset	validation				
	CTRATE	INSPECT		RADCHEST	
		shared	unique	shared	unique
CTRATE	0.8255	0.7505	0.5872	0.7933	0.539
CTRATE+INSPECT	0.829	0.6896	0.735	0.79	0.5896
CTRATE+INSPECT+SEG	0.8291	0.7302	0.7412	0.7904	0.6174
CTRATE+RADCHEST	0.8278	0.7432	0.5714	0.8234	0.748
CTRATE+RADCHEST+SEG	0.8321	0.7692	0.5777	0.8205	0.7298
CTRATE+SEG	0.8305	0.746	0.5867	0.785	0.5589

Table 5. Area under precision recall curve. Model initialized by PubMedBert

model	training dataset	validation				
		CTRATE	INSPECT		RADCHEST	
			shared	unique	shared	unique
Uniferum	CTRATE	0.5583	0.7317	0.1677	0.5274	0.1617
	CTRATE+INSPECT	0.5377	0.7247	0.2949	0.5171	0.1565
	CTRATE+INSPECT+SEG	0.5543	0.7221	0.2998	0.5486	0.165
	CTRATE+RADCHEST	0.5505	0.747	0.172	0.5701	0.2566
	CTRATE+RADCHEST+SEG	0.5565	0.7671	0.1703	0.5862	0.2452
	CTRATE+SEG	0.5557	0.7555	0.18	0.5408	0.1476
	INSPECT	0.2859	0.6023	0.2661	0.2552	0.109
	RADCHEST	0.3588	0.668	0.1259	0.4587	0.1848

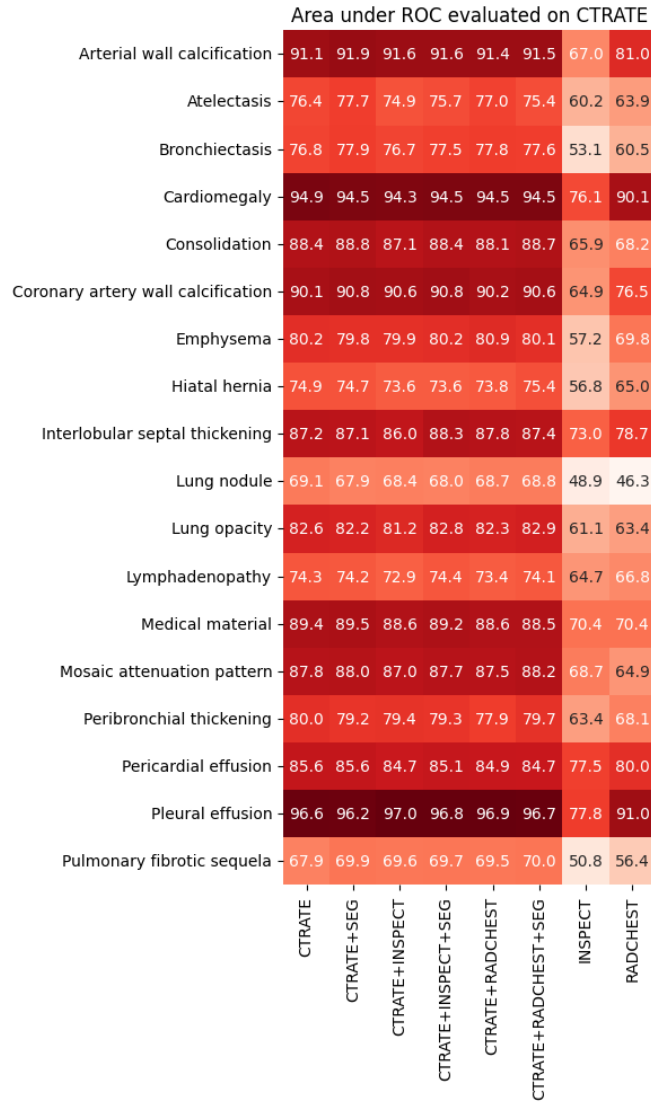


Figure 1. AUROC heatmap on CTRATE. The x-axis represents different training datasets, while the y-axis corresponds to the target classes. Color intensity indicates the area under the ROC curve (AUROC), with higher values reflecting better classification performance.

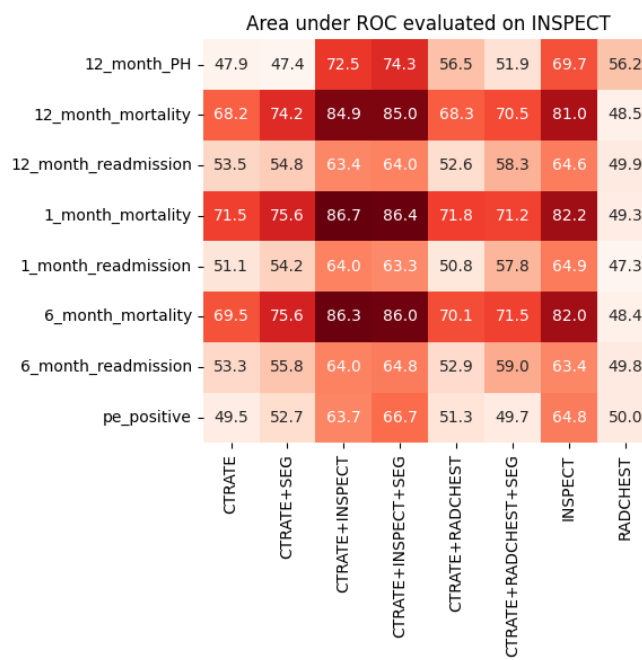


Figure 2. AUROC heatmap on INSPECT. The x-axis represents different training datasets, while the y-axis corresponds to the target classes. Color intensity indicates the area under the ROC curve (AUROC), with higher values reflecting better classification performance.

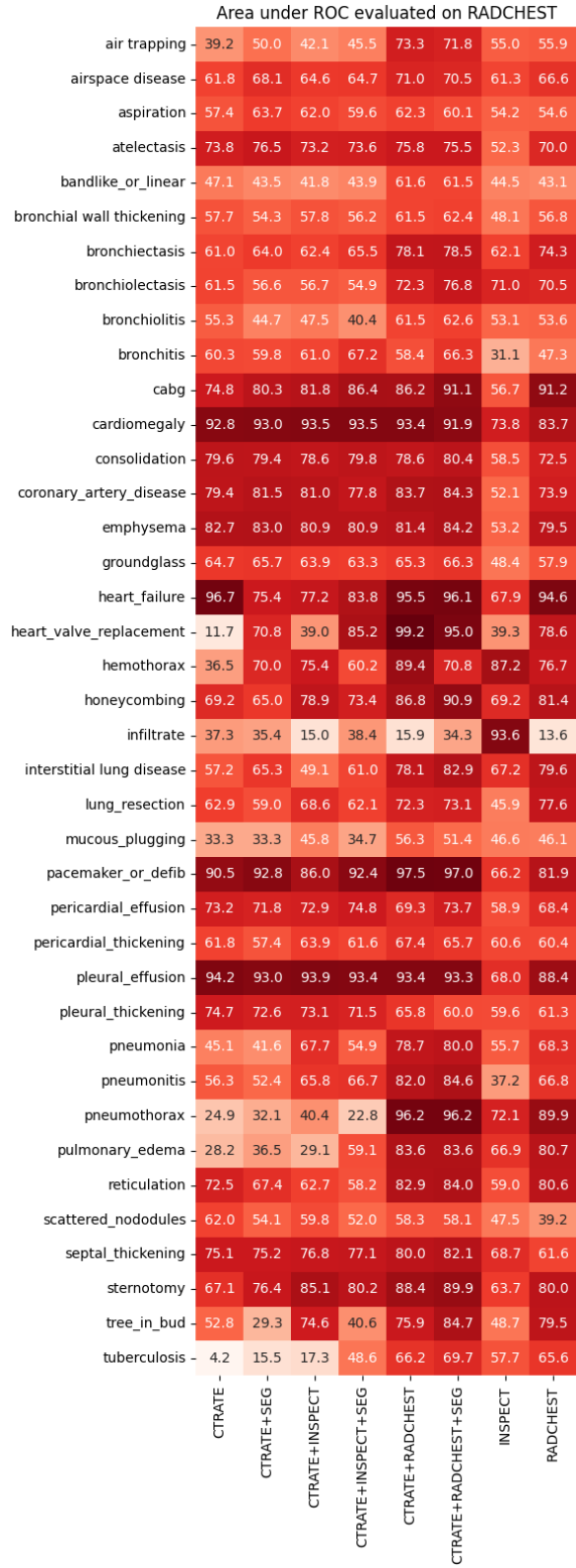


Figure 3. AUROC heatmap on RADCHEST. The x-axis represents different training datasets, while the y-axis corresponds to the target classes. Color intensity indicates the area under the ROC curve (AUROC), with higher values reflecting better classification performance.